Research Square

Preprints are preliminary reports that have not undergone peer review.
They should not be considered conclusive, used to inform clinical practice,
or referenced by the media as validated information.

Superchrons set the visibility of the paleomagnetic record

Mathew Domeier

mathewd@geo.uio.no

Centre for Planetary Habitability, University of Oslo

Leandro Gallo

Centre for Planetary Habitability, University of Oslo https://orcid.org/0000-0002-8124-7536

Thales Pescarini

Institute of Astronomy, Geophysics, and Atmospheric Sciences, University of Sao Paulo

Justin Tonti-Filippini

Centre for Planetary Habitability, University of Oslo https://orcid.org/0000-0003-4091-1223

Physical Sciences - Article

Keywords:

Posted Date: November 23rd, 2026

DOI: https://doi.org/10.21203/rs.3.rs-11788644/v1

License: This work is licensed under a Creative Commons Attribution 4.0 International License.
Read Full License

Additional Declarations: There is **NO** Competing Interest.

Superchrons set the visibility of the paleomagnetic record

Mathew Domeier[1]*, Leandro C. Gallo[1], Thales Pescarini[2,3], Justin Tonti-Filippini[1]

[1]Centre for Planetary Habitability (PHAB), University of Oslo, Norway

[2]Department of Earth and Planetary Sciences, Yale University, USA

[3]Institute of Astronomy, Geophysics, and Atmospheric Sciences, University of São Paulo, Brazil

Abstract

Earth's magnetic field has changed polarity thousands of times throughout its history, but at highly irregular rates, ranging between intervals with rapid polarity switching to geomagnetic superchrons lasting for tens of millions of years [1]. Although reversal frequency is central to understanding the geodynamo and there has long been debate about its relationship to the strength of the field [2], a possible direct influence of the polarity history on the preservation of the observable paleomagnetic record itself has been little considered. Yet secondary magnetizations ('remagnetizations') from multiple continents appear concentrated in intervals associated with superchrons. Here we propose that this pattern arises because remagnetization processes are often protracted, allowing geomagnetic reversals to suppress the net magnetization with an efficiency tied to the reversal frequency and the balance of time spent in the alternating polarity states. This implies that the known paleomagnetic record is biased by geomagnetic reversal history, but also that extensive hidden magnetic histories may be recoverable from nano-scale magnetic dissection of remagnetized rocks.

Main

Records of Earth's geomagnetic field preserved in rocks underpin our understanding of the history of plate tectonics and the evolution of the field itself, but this record is fragmentary and complex. A common problem is that the original magnetization of a rock (acquired when the rock formed) can be obscured or entirely replaced by younger, secondary magnetizations [3–6]. Remagnetizations are usually treated as a nuisance to be excised, but they can preserve valuable information about the ancient geomagnetic field. However, they are infrequently utilized because the specific processes responsible for their acquisition are often difficult to constrain, leaving their timing and duration uncertain. A better understanding of remagnetization mechanisms could thus unlock new opportunities to further unravel Earth's paleogeography and the history of the geomagnetic field.

A remarkable aspect of the paleomagnetic record that remains under-explored is an apparent correlation between the timing of widespread remagnetization events and the occurrence of geomagnetic superchrons. As an example, we consider the paleomagnetic record derived from carbonate rocks (which are relatively susceptible to remagnetization [7]) from Laurentia (Fig. 1). We extract all the carbonate-based paleomagnetic poles from this continent cataloged in the Global Paleomagnetic Database [8] and construct a spherical kernel density estimate to compare against the Phanerozoic apparent polar wander path (APWP) of Laurentia [9] (see Methods). Qualitatively, three high-density regions can be recognized from the kernel density estimate, which are substantiated by a cluster analysis that identifies three pole clusters with directional means proximal to the Early-Middle Ordovician (480-470 Ma), Permo-Carboniferous (300-290 Ma) and mid-Cretaceous (100 Ma) segments of the reference APWP, respectively. These ages closely correspond to the temporal mid-points of the three known geomagnetic superchrons of the Phanerozoic: the Moyero (∼485-466 Ma) [10, 11], Kiaman (∼318-266 Ma) [12, 13], and Cretaceous Normal Superchron (CNS; ∼121-83 Ma) [14]. We further observe that the Kiaman Superchron is especially protracted and the kernel density estimate about the Permo-Carboniferous cluster is correspondingly stronger and wider. Similar apparent relationships between remagnetization episodes in sedimentary rocks and superchrons can be seen in the paleomagnetic records of other continents as well (Extended Data Figs. 1–2).

*Corresponding author: mathewd@geo.uio.no

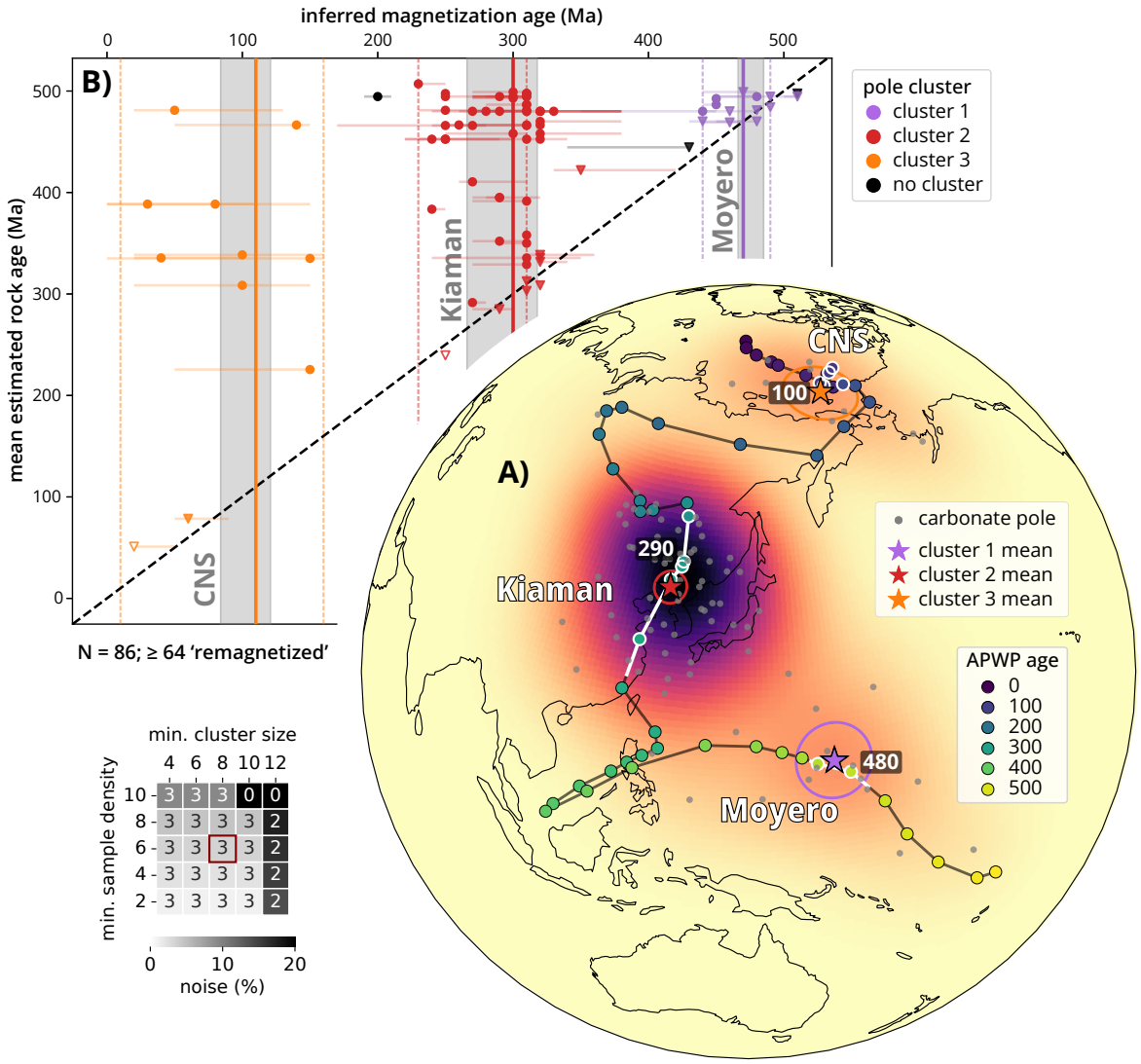

Figure 1: Spatiotemporal distribution of carbonate paleomagnetic poles from Laurentia. A) Spherical kernel density estimate (warm-colored background) of carbonate paleomagnetic poles (grey points) and Fisher directional means (stars with A_{95} confidence circles) from cluster analysis on these poles, compared against the Laurentian apparent polar wander path (APWP; colored circles). White segments of the path/reference poles denote the temporal ranges of the Moyero, Kiaman and Cretaceous Normal superchrons (CNS). Left inset panel shows number of clusters discovered and associated noise according to alternative cluster analysis parameters (maroon frame shows parameters used). **B)** Comparison of mean estimated ages of the rocks hosting the poles in A) vs. the best-estimate of the magnetization age based on a comparison of the pole positions against the reference APWP (see Methods). The individual poles are colored according to their cluster membership, and horizontal lines span valid magnetization ages according to APWP comparisons. Circles denote poles whose oldest valid magnetization age is younger than the age range of the host rock (e.g. remagnetized results). Downward triangles mark all other poles (e.g. possibly primary magnetizations). Open symbols show results with dual-polarities that pass a reversal test. The dashed diagonal line denotes a 1:1 age relationship. Grey intervals show the age range of superchrons, and vertical solid lines show the best-estimated age of the cluster means as determined from comparison against the reference APWP; dashed lines show the upper and lower age range of reference poles within 15° of the cluster means.

We postulate that this conspicuous synchroneity reflects a mechanistic link, where reversal frequency and the relative time spent in alternate polarity states jointly modulate bulk secondary magnetizations acquired on multi-million year time-scales. In this model, the protracted acquisition of remanence across repeated geomagnetic polarity reversals leads to substantial magnetization cancellation, suppressing the measurable bulk remanence of a standard paleomagnetic sample ($\sim$10 cm^3 with $>> 10^6$ ferromagnetic grains [15]). During a geomagnetic superchron, no cancellation occurs and the bulk magnetization grows monotonically, so its final strength scales with the fraction of remanence acquired within the fixed polarity interval. In the following, we show that there are at least two common remagnetization mechanisms in sedimentary rocks that can operate over such multi-million year timescales, and which may act in sequence to further extend the effective temporal window of secondary remanence acquisition and thus exacerbate this reversal history bias.

Chemical remagnetization via clay diagenesis

The remagnetization of carbonate rocks has often been linked to the authigenic growth of magnetite, resulting in the acquisition of a chemical remanent magnetization (CRM) [16]. The generation of authigenic magnetite has been ascribed to various processes, including the migration of orogenic fluids [4, 17] and the maturation of organic matter [18, 19], but the role of clay diagenesis has been increasingly recognized as a widespread agent of carbonate chemical remagnetization [20–23]. Specifically, the transformation of detrital smectite to illite, which requires only modest heating and a source of potassium as a reactant, is associated with the release of iron that can be incorporated into authigenic iron oxides [24, 25]. Importantly, this process can occur within a closed system where there is a local source of potassium and heat provided by sedimentary burial [23]; smectite-bearing successions could therefore be expected to acquire some degree of chemical remagnetization during burial.

To explore how much time may be integrated by a diagenesis-induced CRM, we extend a smectite illitization model [26, 27] to approximate authigenic magnetite growth and CRM acquisition during progressive sedimentary burial (see Methods). This model describes illitization via a simple kinetic reaction that is regulated by the amount of smectite, the availability of potassium, and the temperature. Although the detailed kinetics and geochemical controls on authigenic magnetite growth associated with illitization remain unknown, the smectite-to-illite transformation involves the release of iron, which provides a physical basis for linking the two processes. As a first-order modelling assumption, we take magnetite production to be proportional to the extent of illitization, but we also test alternative responses as a sensitivity test. We further assume that as illitization proceeds, the liberated iron contributes to an evolving magnetite population through both growth of existing grains and formation of new ones [28]. This is consistent with observations that magnetite grains in remagnetized carbonates commonly span a range of magnetic particle sizes, from superparamagnetic (SP) to single-domain (SD) [7]. Because a CRM is acquired when ferromagnetic grains cross a threshold volume that stabilizes their magnetization against thermal fluctuations [16], CRM acquisition itself may be associated to the smectite illitization rate.

Our simulations begin with a parcel of smectite-bearing sedimentary rock at the Earth's surface that is progressively heated through burial according to a prescribed burial rate and geothermal gradient (Extended Data Table 1). Once the temperature exceeds 57.4°C, smectite begins to transform to illite, releasing iron and allowing for authigenic magnetite growth. With progressive burial and heating, illitization continues until smectite is exhausted, the reaction approaches equilibrium, or the system reaches 300°C. This upper temperature limit was selected because it coincides with the approximate lower boundary of greenschist facies conditions, and paleomagnetic studies are rarely conducted on higher-grade sedimentary rocks (and we are only concerned with the possible pre-history of paleomagnetic targets). Considering a range of sedimentary burial rates plausible for a foreland basin setting [29] and geologically constrained estimates for potassium availability [27] (Extended Data Table 1), we observe that the illitization process (operating within the temperature range here considered) can span several tens of millions of years (Extended Data Fig. 3), although it proceeds at a non-linear rate.

Using our adopted proportional acquisition response, we estimate the potential growth of a CRM from the rate of smectite decay. To consider the integrated bulk remanence that would result from such a temporally non-linear acquisition process under a reversing field, we construct a series of stochastic polarity histories for the modelled CRMs to grow in (see Methods). Each polarity history is a sequence of alternating polarity chrons whose durations are drawn at random from a log-normal distribution

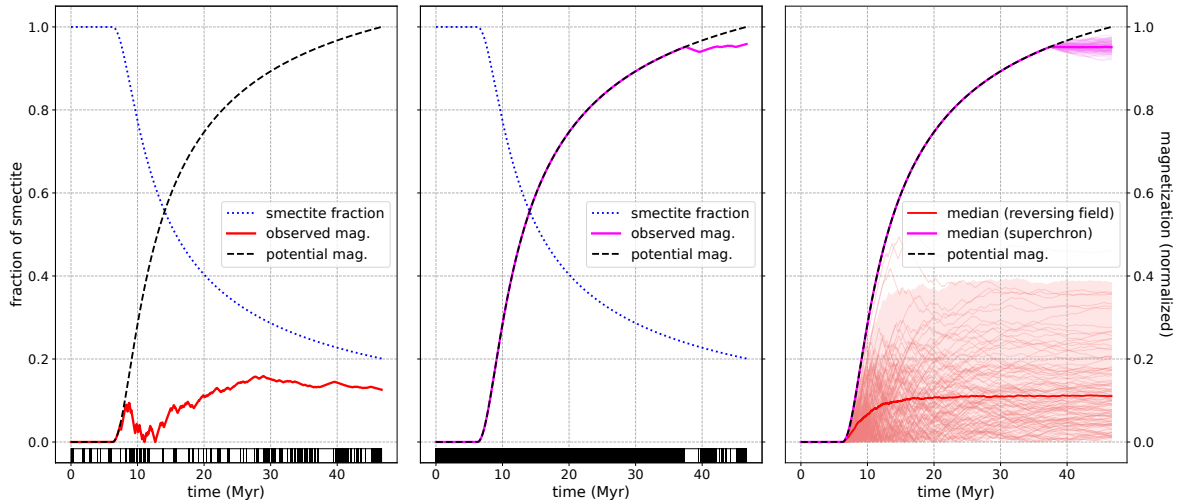

Figure 2: Effect of geomagnetic reversal history on bulk chemical remanent magnetization (CRM) strength. The left two panels show the CRM acquired under our reference model and in association with the synthetic geomagnetic reversal history shown at the bottom of each panel. Dotted blue curves indicate the fraction of smectite remaining. Dashed black curves show the potential CRM that would accumulate under constant polarity; light red curves show the integrated CRM acquired under the imposed polarity history. The right panel shows a Monte Carlo ensemble of 1000 paired polarity histories for the same illitization history. Each pair shares a stochastic background reversal history, but with a prescribed superchron imposed on one history. This pairing isolates the effect of the imposed superchron from differences among the background polarity histories. Thick curves show the ensemble medians. All models are run with the reference values in Extended Data Table 1.

fitted to the observed chron durations of the geomagnetic polarity timescale (GPTS) since 171 Ma [14] (Extended Data Fig. 4). Treating the field direction as fixed apart from its polarity over the acquisition interval, we compute the increment of CRM accumulated in each chron and use the polarity to assign a sign (± 1) to the remanence contribution. The summation of all signed increments gives the expected bulk magnetization under that polarity history, which we normalize by the total potential magnetization (the summation of the absolute values of each remanence contribution) (Fig. 2). Repeating this process N=1000 times under stochastic histories of a reversing field, we collect an ensemble of results that show that the final bulk CRM represents a small fraction of the potential CRM (Fig. 2c). A paired experiment that replaces the first 37.5 Myr of the polarity history with a superchron (the approximate duration of the CNS) results in a bulk remanence that is nearly an order of magnitude stronger that that acquired under a reversing field. Variations on the parameters used in our reference model demonstrate that this outcome is not strongly sensitive to the acquisition response, burial rate, or potassium availability (Extended Data Fig. 5a-d), whereas variations on the onset timing and duration of the imposed superchron have a strong effect on the bulk remanence acquired (Extended Data Fig. 5e-f). These results suggest that the protracted CRMs acquired outside a superchron are susceptible to significant suppression, and their net remanence may be challenging to detect from standard bulk sample measurements. It furthermore suggests that secondary magnetizations may be more widespread than presently recognized.

Thermoviscous remagnetization during exhumation

As an alternative to the CRM model, some widespread carbonate remagnetization events have been ascribed to the acquisition of thermoviscous remanent magnetizations (TVRMs) associated with regional exhumation and cooling [30–33]. The magnetization of all ferromagnetic particles evolves through thermally-activated relaxation towards equilibrium with the external magnetic field, with a characteristic relaxation time that depends exponentially on temperature, as well as on grain size, shape and magnetic anisotropy [34, 35]. Magnetic relaxation is rapid at elevated temperatures but slows dramatically during cooling, so the moments of individual magnetic grains in a cooling system can become blocked as their relaxation times exponentially increase. Given that natural magnetic grain populations exhibit a distri-

bution of grain sizes (and so blocking temperatures) and regional exhumation histories can proceed over tens of millions of years, the acquisition of an exhumation-related TVRM could also be expected to be temporally protracted.

To explore how much time may be integrated in exhumation-related TVRMs, we employ Néel theory [34, 35] and model the magnetic moments of non-interacting, single-domain magnetite grains in a system undergoing cooling. Larger grains (vortex and multi-domain grains) are not included in our model, as they require dedicated micromagnetic treatment for a complete accounting of their multiple metastable states and energy barriers [36, 37]. However, this is a reasonable simplification because carbonates that have been subjected to sedimentary burial and diagenesis are commonly dominated by SP to SD magnetite [7]. We represent the magnetic carriers in our model with a log-normal distribution of grain volumes, weighted by grain number. In our reference model, the median volume of this distribution corresponds to a grain with an equivalent spherical volume diameter of 35.5 nm, and it has a standard deviation (log volume) of 0.30 (Extended Data Table 1; Extended Data Fig. 6). These distribution parameters were selected to sample the thermally active blocking window during cooling rather than to mimic any specific measured granulometry, but we also conduct variations on these parameters as sensitivity tests (Extended Data Fig. 7a,b).

Our simulations track the viscous magnetic evolution of each grain volume as the system undergoes exhumation and progressive cooling from 300°C to ambient surface conditions (20°C). For our reference model, we use an exhumation rate of 0.2 mm/yr and a geothermal gradient of 30°C/km, yielding a cooling rate of 6°C/Myr (Extended Data Table 1). This is comparable to post-orogenic cooling of foreland basins [38, 39] and to the fastest exhumation pulses documented in cratons [40], whereas cratonic interiors and intracratonic basins typically cool at 0.1–1°C/Myr over hundreds of millions of years [41]. As for our CRM experiments above, we pair this TVRM acquisition model with synthetic polarity histories to consider how the resulting bulk sample magnetization may be modulated by reversal frequency and polarity bias. In each simulation, we follow the blocking criterion for continuous cooling of Dodson & McClelland-Brown [42] to estimate the blocking temperatures of individual grain volumes, below which their magnetic alignment remains frozen while their moment magnitude can change. At the start of each simulation, the grains are all assumed to be at equilibrium with the external field, and grain volumes that are blocked at the initial temperature are excluded from the analysis. As before, the sign of each contribution of remanence is assigned according to the corresponding chron under a given polarity history, and the bulk TVRM is normalized by the potential TVRM (acquired under a fixed polarity field). We generate N=1000 alternative paired polarity histories (with/without a superchron) to enable statistical assessment (Fig. 3).

Our results firstly demonstrate that the acquisition of a TVRM can occur over several tens of millions of years. In contrast to the CRM case, where the simulations begin with no remanent magnetization, the TVRM case begins with all the grains in magnetic equilibrium because they are in an SP state. As the system cools the total potential magnetization grows owing to the inverse relationship between saturation magnetization and temperature, but the trend shallows as cooling progresses. When these TVRMs are acquired under a reversing field regime and integrated, we again observe that the net remanence, as would be measured in a bulk sample, is invariably a small fraction of the magnetization that would be acquired under a non-reversing field (Fig. 3).

Remagnetizations in series

The results of the CRM and TVRM models reveal that both types of magnetizations can be acquired on timescales of several tens of millions of years. However, these remagnetization processes can also occur in series, further lengthening the overall interval of magnetization acquisition. To explore this, we model a sedimentary system that undergoes sedimentary burial and heating up to 300°C and then exhumation and cooling back to 20°C. Adopting the parameters from our reference CRM and TVRM models (Extended Data Table 1), this gives rise to a ∼100-Myr heating-cooling cycle, in which a CRM is acquired over the first half and a TVRM over the second half. For simplicity, we assume that grains which acquire a CRM become sufficiently large to remain blocked at 300°C, such that the subsequently acquired TVRM is hosted by a distinct population of grains and the CRM remains fixed during cooling. For ease of comparison, we also assume that the potential bulk magnetization of both the CRM and TVRM reach parity by the end of the 100 Myr simulation.

To consider the role that the reversal history could play in the resulting CRM and TVRM magnitudes,

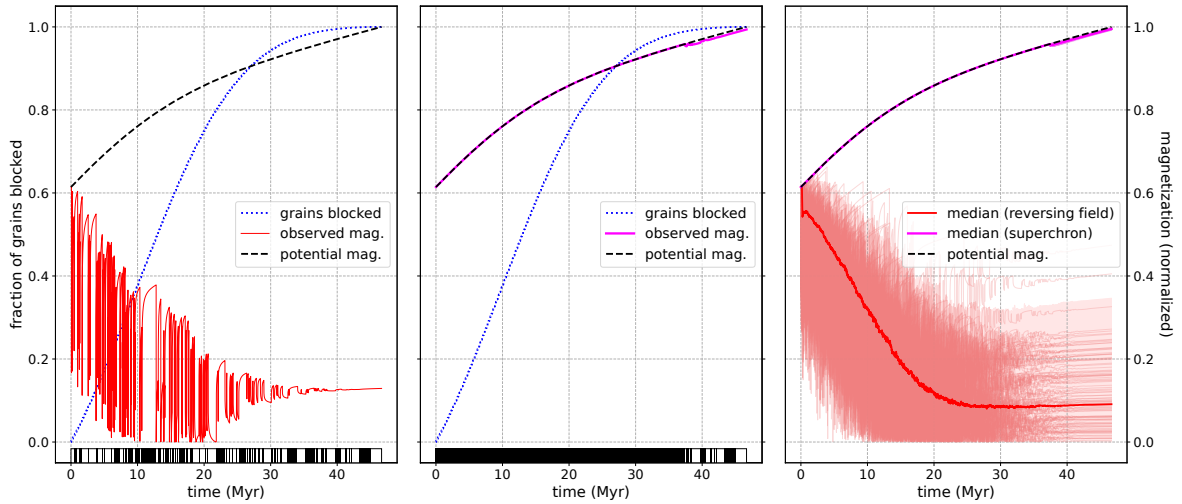

Figure 3: Effect of geomagnetic reversal history on bulk thermoviscous remanent magnetization (TVRM) strength. The left two panels show the TVRM acquired in association with the synthetic geomagnetic reversal history shown at the bottom of each panel. The dotted blue lines in both panels show the fraction of grains blocked as exhumation-related cooling proceeds. The dashed black line shows the potential TVRM that would accumulate under constant polarity; the red lines show the integrated TVRM acquired under the imposed reversal history. The panel on the right shows a Monte Carlo ensemble of 1000 paired polarity histories for the same cooling history. Each pair shares a stochastic background reversal history, but with a prescribed superchron imposed on one history. This pairing isolates the effect of the imposed superchron from differences among the background polarity histories. The thick line is the median result from the ensemble. All models are run with the reference values in Extended Data Table 1

we impose two distinct 50 Myr stochastic polarity histories on the heating and cooling cycles. A 50 Myr 'hyper-reversing' history is first generated by resampling the GPTS chron duration distribution as before (Extended Data Fig. 4), but we divide each sampled chron by a factor of 5 to represent a hyper-reversing regime. A companion 50 Myr 'biased' history is constructed by again sampling from the GPTS chron duration distribution, but between 0 and 25 Myr we adjust the duration of the normal and reverse chrons to make the former a factor of 5 longer than the latter; this yields a polarity history with approximately the same average switching rate, but with more time spent in the normal polarity state. We generate N=1000 paired hyper-reversing and biased polarity histories and impose both combinations of these paired histories on the adjoined CRM-TVRM models (Fig. 4).

The results further demonstrate that the geomagnetic reversal history largely dictates the strength of the secondary magnetizations acquired. In the biased to hyper-reversing history (Fig. 4a), we observe that the net CRM is relatively strong and the subsequently acquired TVRM is highly suppressed, whereas the opposite is true where the polarity histories are reversed (Fig. 4b). These results also highlight that the field need not be in a strictly non-reversing regime to augment a magnetization, as a polarity bias will strengthen a magnetization in proportion to the time-spent in a single polarity state over the acquisition interval. Similarly, the hyper-reversing regime suppresses the magnetization even beyond that of a normal reversing regime, because the likelihood of vector cancellation increases with the reversal frequency. This simple experiment also underscores how inferences on the magnetic history of a rock (e.g. whether apparently carrying a CRM, a TVRM, or no detectable secondary remanence at all) can be skewed by the reversal history itself.

A hidden paleomagnetic record

The temporal clustering of remagnetizations across multiple independent cratons requires an explanation that is both global and synchronous. We contend that the most parsimonious explanation is that remagnetization processes are protracted: bulk secondary magnetizations acquired under a reversing field regime tend to self-cancel and often go undetected. We have demonstrated that there are at least

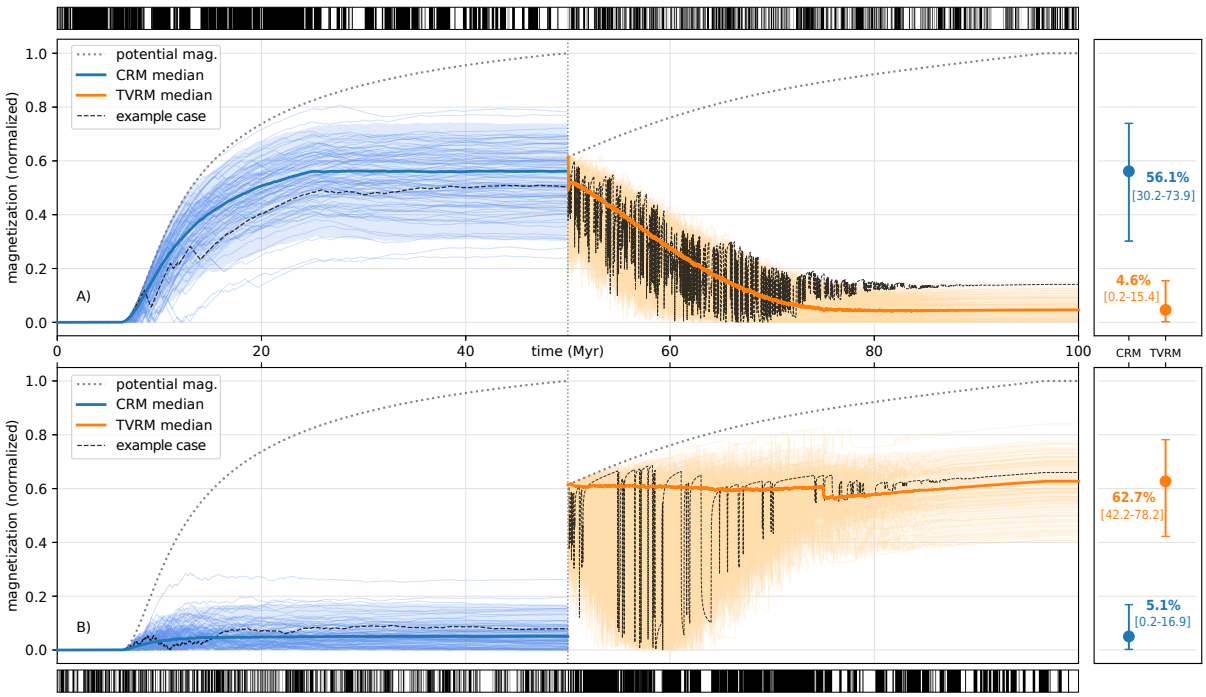

Figure 4: Effect of geomagnetic reversal history on the bulk CRM and TVRM in a remagnetization series. Both panels show the acquisition of a CRM (blue curves; during 50 Myr of heating) and a TVRM (orange curves; during 50 Myr of cooling) under 1000 stochastic polarity histories. In the upper panels, the first 50 Myr includes a 25 Myr 'biased' interval where the field spends 5x more time in the normal polarity state, but otherwise reverses at an average rate. The second 50 Myr polarity interval has a 5x greater reversal frequency, and reflects a hyper-reversing regime. In the lower panels, the same 1000 stochastic polarity histories are used, but the order of the biased and hyper-reversing series is reversed. The thin blue and orange curves in each panel show individual results, and the thick blue/orange curves show the corresponding medians. The thin dashed black lines show one example run from each panel, which corresponds to the specific polarity history shown as bars above and below the main panels. The dotted gray lines in all panels show the potential CRM/TVRM that would be aquired in a static field. The thin panels to the right show the median net CRMs and TVRMs at the end of the simulation, and the central 95 percentile range of the individual results. All models are run with the reference values in Extended Data Table 1 (except those pertaining to the polarity history).

two common remagnetization mechanisms that can plausibly operate on multi-million year timescales, without excluding the possibility of there being others. The two mechanisms examined can moreover act in sequence, extending the overall integrated time window, and exacerbating the bias toward intervals dominated by a single geomagnetic polarity. This explanation thus avoids the need to invoke an episodic enhancement of the processes responsible for remagnetization (e.g. fluid migration, diagenesis, or burial and exhumation rates), which otherwise must have repeatedly coincidentally occurred in concert with superchrons to explain their synchroneity. This reframes a widely held view that regional remagnetization episodes are controlled by the timing of major phases of orogenesis [4, 32, 33, 43, 44]: orogenesis helps govern the conditions and timing of magnetization acquisition (via burial, exhumation, and the transmission of fluids), but reversal history dictates its net paleomagnetic expression and thus ultimately its dectectability.

Our results also highlight an important caveat for attempts to date remagnetizations. Several studies have suggested that the age of CRMs acquired via clay diagenesis could be determined through the radiometric dating of authigenic illites [45, 46]. However, our results indicate that such a CRM could have been acquired over several tens of millions of years. The authigenic illite in such rocks would then comprise several generations, as is commonly observed in grain-size dependent illite ages from diagenetic settings [47, 48], and a bulk date would return only their mass-weighted average. Consequently, future attempts to date diagenetically-induced CRMs should seek to resolve the full range of illite formation ages, through grain-size fractions or in situ dating of texturally distinct populations, and evaluate them in

conjunction with the geomagnetic polarity history. The results of our TVRM models likewise suggest that any attempt to date a TVRM via thermochronology requires the full temperature–time path, evaluated against the possible blocking and polarity histories.

A particularly intriguing implication of this work is that if protracted CRMs and TVRMs are commonly suppressed at the bulk rock scale, then many temporally extensive secondary magnetic histories may remain effectively hidden in remagnetized rocks (which may not even be recognized to be carrying a secondary remanence). In some specific instances, very high-resolution thermal demagnetization has enabled the isolation of opposed TVRMs [49, 50]. However, because magnetic blocking occurs over a range of temperatures, in a slowly cooled system magnetization vector cancellation can occur even within the same grain size population, making the subsequent dissection of the constituent magnetic vectors impossible by standard thermal demagnetization. Similarly, interfering CRMs acquired by authigenic magnetite growth may be hosted by grains with otherwise identical thermal and coercive stability spectra, making their separation intractable by conventional bulk methods. However, as stepwise CRM acquisition is related to progressive grain growth, there may be a relationship between grain size (or proximity to reactants) and magnetization age. This prediction provides a novel motivation for ongoing developments in micro- and nano-scale paleomagnetic techniques that seek to resolve magnetic moments at the grain-scale [51–53]. If the mechanisms explored here are widespread, such approaches may reveal far more complex magnetic populations at the grain scale than presently anticipated, but also ones that could be dissected to recover temporally extensive records of Earth's paleomagnetic history.

Methods

Analyses of paleomagnetic pole compilations

To illustrate the apparent correlation between widespread sedimentary remagnetization episodes and the occurrence of geomagnetic superchrons, we interrogated paleomagnetic records cataloged in the Global Paleomagnetic Database [8]. We extracted all records with sampling sites that fell within three different Phanerozoic continents: Laurentia, Baltica and Amazonia, using the delineations of those continents by [54]. These continents were chosen because they have a relatively high number of Phanerozoic paleomagnetic records enabling largely complete definitions of their Phanerozoic apparent polar wander paths (APWPs), and we adopt the spline reference APWPs of Laurentia and Baltica of [9]. For Amazonia we utilize the APWP of Gondwana, rotated into the Amazonian reference frame. For each of the three paleomagnetic compilations, we extracted all entries derived from sedimentary rocks less than 720 Ma (as polarity determinations for older records become ambiguous; see below), and discarded entries taken from unpublished sources. We then attempted to determine the polarity of each reported pole position (not explicitly reported by the GPDB) by comparing both the reported pole and its antipode to the corresponding reference APWP and selecting the option with the shortest arc distance to the APWP. Because the Phanerozoic APWPs of these three continents are largely restricted to a single hemisphere, this yields unambiguous polarity determinations for Phanerozoic magnetizations. We then discard all paleopoles that fall more than 15° from any part of the reference APWPs (to exclude pre-Phanerozoic magnetizations, structurally rotated poles, or otherwise pathological data). For Baltica and Amazonia, this yields 197 and 66 sedimentary paleomagnetic poles, respectively. Because the Laurentian compilation is relatively larger, we further extract from that dataset the poles derived from carbonate rocks (which are relatively easily remagnetized), yielding 86 paleomagnetic records.

We estimate the likely magnetization age of each retained pole as the age of the reference pole that it falls closest to (and which is no older than the maximum reported age of the host rock itself). For any candidate pole that contributes to the underlying APWP, we first exclude the pole from the basis data supporting the APWP and rebuild the path before conducting the comparison to avoid circularity in these age assignments. We further estimate the valid magnetization age range for each candidate pole by finding the oldest and youngest reference poles the candidate pole is statistically indistinct from. To accomplish this, we follow the B_{95} approach of [55]. In this approach, for a candidate pole comprised by N virtual geomagnetic poles (VGPs), we recalculate each reference pole in the APWP by randomly drawing N VGPs from a pool of parametrically resampled VGPs from the constituent basis poles contributing to the reference pole. The reference pole is then recalculated from these N VGPs, and this process is repeated 1000 times, giving 1000 realizations of the reference pole position. From this ensemble of reference pole positions, the mean of means is determined, as well as the B_{95}, which is the angular radius from the mean of means which contains 95% of the realized means. With this, we then assess whether the candidate pole is statistically distinguishable from that reference pole, according to their quadrature sum:

$$gcd < \sqrt{A_{95,\mathrm{can}}^2 + B_{95,\mathrm{ref}}^2} \tag{1}$$

where gcd is the great circle distance between the mean of the candidate pole and the reference pole, $A_{95,\mathrm{can}}$ is the 95% cone of confidence of the candidate pole, and $B_{95,\mathrm{ref}}$ is the $B_{95,\mathrm{ref}}$ of the reference pole. This is then repeated for each reference pole of the APWP (younger than the maximum age of the host rock of the candidate pole), and the estimated valid magnetization age range is then the age range between the oldest and youngest reference poles where this criterion is passed. Where the reference pole is interpolated, we instead use $gcd < 15°$ as the cutoff. Where paleomagnetic entries lack a specification of N or $N < 6$ we use the number of samples; where this is not available we adopt $N = 10$ (the approximate median value of the compilation). Where A_{95} is unreported, we estimate it from the reported DP/DM; where these are not available we adopt $A_{95} = 5°$ (the approximate median value of the compilation).

In Fig. 1 and Extended Data Figs. 1 and 2 we plot the inferred magnetization ages of each pole against the mean estimated age of their host rocks. Rocks preserving a primary magnetization should fall along the unit slope, whereas remagnetized rocks will lie above this line. In all three panels, we observe that many of the records appear to correspond to remagnetizations, and that the inferred ages of these remagnetizations appear concentrated in several bands which correspond to the timing of the Moyero,

Kiaman and Cretaceous Normal superchrons. To further evaluate this qualitative assessment, we construct spherical kernel density estimates (KDE) from these data, and perform spatiotemporal cluster analyses on them using the HDBSCAN algorithm as implemented in the scikit-learn library [56]. For the latter, we consider a range of minimum cluster size and sample density thresholds, and include a minor age weighting (where a 50 Myr age separation is equivalent to a 10° separation) to enable possible segmentation between recurrent segments of the APWPs. On the basis of cluster membership, we then compute Fisher means for each cluster and determine the range of reference poles which fall within 15° of these cluster means. These analyses reinforce that there exists three persistent pole clusters with means proximal to the Early-Middle Ordovician, Permo-Carboniferous and mid-Cretaceous segments of the reference APWPs (Fig. 1, Extended Data Figs. 1 and 2). Many of these pole clusters include a substantial number of remagnetized poles. A fourth, mid-Paleozoic pole cluster also appears in Baltica (ca. 430 Ma), but is mostly associated with likely primary poles.

Stochastic polarity histories

Stochastic polarity histories are constructed by randomly drawing polarity chron durations from a log-normal distribution fitted to the observed polarity chron durations of the last 171 Ma, as estimated in the geomagnetic polarity timescale of Ogg [14]. Before fitting, chron C34 (the Cretaceous Normal Superchron; approximately 121–83 Ma) was removed to characterize chron durations outside superchron intervals. The resulting distribution (natural logarithm of chron durations expressed in Myr) has a fitted mean of -1.86 and standard deviation of 1.08 (Extended Data Fig. 4), corresponding to a median chron duration of 0.156 Myr and a geometric standard deviation of 2.94. To construct stochastic polarity histories, successive sampled durations define chron boundaries, with alternating normal and reversed polarities, which we add in sequence beginning with normal polarity at $t = 0$. To evaluate the effect of superchrons, each stochastic history is paired with an otherwise identical history in which normal polarity is imposed over some interval of the original history, with prescribed onset time and duration. For all our simulations, we generate an ensemble of $N = 1000$ such paired histories to quantify the variability in modelled remanence arising from individual stochastic polarity histories.

Chemical remanent magnetization via illitization

To model CRM acquisition via clay diagenesis we employ the smectite illitization model of Cuadros & Linares [26], which expresses the process with the kinetic equation:

$$-\frac{dS}{dt} = k(T) K_e^m S^n \tag{2}$$

where S is the proportion of smectite layers in mixed-layer clay, k is a temperature-dependent rate constant, and K_e is an effective measure of the availability of potassium for illitization. For constant temperature, this equation has the analytical solution:

$$S(t) = \left[S_0^{1-n} \; - \; (1-n)\, k(T)\, K_e^m\, t \right]^{\frac{1}{1-n}} \tag{3}$$

Following Cuadros & Linares [26], we adopt $m = 0.25$ and $n = 5$ for these exponents. Cuadros [27] fit $k(T)$ with a quadratic temperature function:

$$k = 1.213 \times 10^{-9} T^2 - 6.608 \times 10^{-8} T - 2.033 \times 10^{-7} \tag{4}$$

This parameterization sets the initiation of illitization above $T \approx 57.4$°C. Through specification of a burial rate and geothermal gradient, we build a thermal history and model progressive illitization by numerically integrating equation (2) using the analytical solution in equation (3) evaluated at each time step. Our simulations run until the temperature reaches 300°C (lower greenschist facies conditions). Our reference model uses a geothermal gradient of 30°C/km and a burial rate of 0.2 mm/yr (Extended Data Table 1). Alternative thermal histories that employ a range of burial rates observed in foreland basin settings (0.1-0.5 mm/yr [29]) are explored as sensitivity tests (Extended Data Fig. 5c). The dominant uncertainty in these models is K_e, but following Cuadros [27], a plausible range of K_e values (10^{-14}–10^{-8}) reproduces observations of smectite content vs. burial depth in various sedimentary basins.

This range of K_e values predicts that illitization will proceed over millions to tens of millions of years, assuming reasonable rates of sedimentary burial (Extended Data Fig. 3). Notably, the smectite profiles used to invert for these K_e values come from clastic successions, and K_e values in carbonate-dominated successions are likely to be lower, given their lower bulk K content and competition from Ca cations in pore waters [27]. We therefore treat these K_e values as an upper bound and use $K_e = 10^{-14}$ in our reference model; lower K_e values will further prolong the illitization process and are explored in a sensitivity test (Extended Data Fig. 5d).

Illitization involves the fixation of K^+ in smectite interlayers, accompanied by a charge-compensating substitution of Al^{3+} for Si^{4+} in the tetrahedral layer [24]:

$$\text{Smectite} + Al^{3+} + K^+ \longrightarrow \text{Illite} + Si^{4+} \tag{5}$$

K is the critical reactant [57], because if Al is immobile the reaction can still proceed through the partial consumption of smectite layers [25]. Although Fe does not explicitly appear in the reaction, detrital smectites contain Fe in their octahedral sheets, and during illitization this Fe is replaced by Al and expelled [58, 59]. However, Boles & Franks [25] suggest that Fe-rich smectites are less reactive than aluminous ones, and that progressive Fe loss may not occur before short-range ordering above 100°C. Quantification of Fe release per mole of smectite transformed is complex, as it depends on the reaction pathway [25], but also because Fe nanophases, which can be adsorbed to the reactive clay surface, may also be liberated during clay diagenesis [21]. Quantification of magnetite authigenesis is likewise complex, as it is sensitive to fluid-rock chemistry, including the redox state, pH, and the presence of competing mineral phases.

Rather than attempting to explicitly budget Fe fluxes during illitization and authigenic magnetite growth, we adopt a simplified approach. We first observe that magnetite particle sizes in remagnetized carbonates are found to comprise a spectrum from SP to stable SD grain sizes. This grain size spectrum suggests that magnetite authigenesis is often temporally distributed, with grains nucleating at different times and growing at variable rates rather than evolving synchronously. The nucleation timing and growth rates of specific grains will be locally controlled by the fluid-rock chemistry, but at the macro-scale the rate of authigenesis is assumed to scale with the availability of Fe liberated by illitization. Accordingly, we assume that the rate of smectite illitization provides a first-order proxy for the rate of magnetite authigenesis, and hence for CRM acquisition, as individual grains grow beyond their blocking volume.

We define the normalized illitization reaction progress as:

$$x_i = \frac{S_0 - S_i}{S_0 - S_f}, \tag{6}$$

where S_0, S_i and S_f are the smectite fractions initially, at timestep i, and at the end of the simulation, respectively. An acquisition function $F(x)$ specifies the fraction of the final potential CRM acquired by a given stage of the reaction progress. Our reference model assumes $F(x) = x$ (proportional acquisition), but we also explore the sensitivity of our results to the use of $F(x) = 1 - (1 - x)^q$ and $F(x) = x^q$, with $q = 2$ or 6, which shift the acquisition to earlier or later stages of the illitization process, respectively (Extended Data Fig. 5a,b).

The normalized magnetization increment at each timestep is thus:

$$\Delta m_i = F(x_i) - F(x_{i-1}) \tag{7}$$

The sign of each increment is determined by the field polarity ($p_i = \pm 1$) at the corresponding timestep, and the increment is retained as fixed thereafter. We thus assume that each increment represents a population of grains that have become magnetically blocked through growth, but without explicitly modelling grain growth, delayed magnetic blocking or subsequent relaxation. The normalized bulk CRM magnitude accumulated by time t_j is:

$$M(t_j) = \left| \sum_{i=1}^{j} p_i \Delta m_i \right| \tag{8}$$

Opposite-polarity contributions cancel, and the normalization gives a final magnitude of unity to a CRM acquired in a fixed-polarity field.

Thermoviscous remanent magnetization

We model thermoviscous remanent magnetization (TVRM) during cooling using the SD theory of Néel [34, 35]. We consider non-interacting, uniaxial grains of magnetite with randomly oriented easy axes. For grains of a given volume V, the mean magnetic moment projected along the field axis is:

$$m = M_s(T)Vq, \tag{9}$$

where M_s is the saturation magnetization and q is a dimensionless measure of the mean alignment of grain moments along the field axis. In a field of magnitude B, the equilibrium alignment is:

$$q_{\mathrm{eq}}(V,T,B) = \int_0^1 u \tanh(au), du, \qquad a = \frac{M_s(T)VB}{k_BT}, \tag{10}$$

where T is absolute temperature, k_B is Boltzmann's constant and u is the cosine of the angle between a grain's easy axis and the field axis. However, the alignment of grain moments is not instantaneous, and they relax towards equilibrium according to:

$$\frac{dq}{dt} = \frac{p(t)q_{\mathrm{eq}} - q}{\tau}, \tag{11}$$

where $p(t) = \pm 1$ is the field polarity and τ is the Néel relaxation time:

$$\tau(V,T) = \tau_0 \exp\left[\frac{K(T)V}{k_BT}\right] \tag{12}$$

Here, $K(T)$ is the temperature-dependent anisotropy energy density and τ_0 is the relaxation prefactor, for which we adopt the value of 10^{-9} s [35].

As the temperature decreases, relaxation times increase and the grain moments become progressively more sluggish in aligning with the external field direction. We can track the evolution of the mean alignment by applying the analytical solution to equation (11):

$$q_{i+1} = (1-r)q_i + r\,p\,q_{\mathrm{eq}}, \qquad r = 1 - \exp\left(-\frac{\Delta t}{\tau}\right), \tag{13}$$

where we hold temperature constant over the timestep Δt, and p, q and τ are evaluated at each timestep. This shows that when $\tau_i \ll \Delta t$, alignment approaches equilibrium, whereas for $\tau_i \gg \Delta t$, the previous alignment is largely maintained. Thus, during cooling, there exists a temperature interval across which the moment alignment becomes blocked. Following Dodson & McClelland-Brown [42], we estimate the blocking temperature T_b relative to the local time it takes for τ to increase by a factor e along the cooling path:

$$\tau(T_b) = 1.78\,\theta, \qquad \theta = \left[\frac{d\ln\tau}{dt}\right]^{-1} \tag{14}$$

Grains that satisfy this criterion at the initial temperature of the simulation ($T_0 = 300°\mathrm{C}$) are excluded, and all the retained grains are set to equilibrium at $t = 0$. As cooling proceeds we track the fraction of grains that become blocked according to equation (14) while evolving their alignment throughout the simulation. The resulting integrated moment of the total population of grains at a given time is:

$$\overline{m}(t) = M_s[T(t)] \sum_k w_k V_k q_k(t) \tag{15}$$

where w are number weights from the prescribed grain size distribution (see below).

We assume that all the grains in our model are magnetite, and that they share the same M_s, which we define relative to a reference value as:

$$M_s(T) = M_{s,\mathrm{ref}}\,\beta(T), \qquad \beta(T) = \left[\frac{1 - T/T_c}{1 - T_{\mathrm{ref}}/T_c}\right]^{\alpha}, \tag{16}$$

where T_c is the Curie temperature that we take as 580°C, and α is a mineral-specific constant. Following Cych *et al.* [60], we set $\alpha = 0.4$ and take $M_{s,\mathrm{ref}} = 4.95 \times 10^5\,\mathrm{A\,m^{-1}}$ as the reference value at $T_{\mathrm{ref}} = 0$°C. We further assume that the magnetite grains have the same form and their anisotropy energy is controlled by shape anisotropy:

$$K(T) = K_{\mathrm{ref}}\,\beta(T)^n, \qquad K_{\mathrm{ref}} = \frac{1}{2}\mu_0\,\Delta N\,M_{s,\mathrm{ref}}^2, \tag{17}$$

where the exponent n describes the scaling of anisotropy with normalized saturation magnetization and is set to 2, as required for fixed-shape magnetostatic anisotropy [35], μ_0 is the magnetic permeability, and ΔN is a constant relating to the grain shape. We set $\Delta N = 0.155$, corresponding to slightly prolate grains with an aspect ratio of ~ 1.52, for which the assumption that anisotropy is shape-dominated is reasonable [60].

We use a log-volume distribution to model the grain population, with a median equivalent spherial volume diameter of 35.5 nm, which is close to the SP-SD threshold at conditions of 300°C, but significantly above the SP-SD threshold at 20°C (Extended Data Fig. 6). The effect of variations on the median location and the width of this distribution are considered among the sensitivity tests (Extended Data Fig. 7a,b). We do not attempt to model vortex or MD grains, as these require dedicated micromagnetic modelling and are not commonly observed in remagnetized carbonates.

Cooling histories are constructed from a prescribed constant exhumation rate and geothermal gradient, and all our TVRM simulations start with an initial temperature of 300°C (lower greenschist facies conditions) and cooling continues until the system reaches 20°C. For our reference model we adopt a geothermal gradient of 30°C/km and an exhumation rate of 0.2 mm/yr, Extended Data Table 1), which yields a cooling rate of 6°C/Myr. This exhumation rate is consistent with estimates from actively inverted foreland basins [38, 39], but a wider range of exhumation rates are considered as a sensitivity test (0.1-0.5 mm/yr; Extended Data Fig. 7d). Slower post-orogenic denudation rates (e.g. [61]) would act to further suppress the net remanence acquired under a reversing field.

The magnitude of the external field B is held fixed in our simulations (although different field strengths have no effect in the low field regime: [Extended Data Fig. 7c], and we change only its sign in accordance with the stochastic polarity history (as in the CRM model). Also as in the CRM model, each polarity history is paired, where the polarity sequence in one of the histories has been replaced with a superchron of prescribed onset and duration. From an ensemble of N=1000 paired simulations, we evaluate the effect of superchrons on the magnitude of the resulting TVRM. Variations on the onset time and duration of the superchron demonstrate that even partial overlap of a superchron with the magnetization acquisition interval will yield a significant increase in the resulting remanence (Extended Data Fig. 7d,e).

Data availability

The paleomagnetic records analysed in this study were obtained from the Global Paleomagnetic Database [8], and the reference apparent polar wander paths were modified from [9], as described in the Methods.

Code availability

The code used to analyse the paleomagnetic records and to simulate remagnetizations will be made available to the editors and reviewers during peer review. All codes will be deposited in a publicly accessible repository upon acceptance of the manuscript, with a link provided in the published article.

References

1. Gallet, Y. & Pavlov, V. Three distinct reversing modes in the geodynamo. *Izvestiya, Physics of the Solid Earth* **52,** 291–296 (2016).
2. Ingham, E., Heslop, D., Roberts, A., Hawkins, R. & Sambridge, M. Is there a link between geomagnetic reversal frequency and paleointensity? A Bayesian approach. *Journal of Geophysical Research: Solid Earth* **119,** 5290–5304 (2014).
3. Creer, K. Palaeozoic palaeomagnetism. *Nature* **219,** 246–250 (1968).
4. McCabe, C. & Elmore, R. D. The occurrence and origin of Late Paleozoic remagnetization in the sedimentary rocks of North America. *Reviews of Geophysics* **27,** 471–494 (1989).
5. Van Der Voo, R. & Torsvik, T. H. The history of remagnetization of sedimentary rocks: deceptions, developments and discoveries (2013).
6. Elmore, R. D., Muxworthy, A. R. & Aldana, M. Remagnetization and chemical alteration of sedimentary rocks (2013).
7. Jackson, M. & Swanson-Hysell, N. L. Rock magnetism of remagnetized carbonate rocks: Another look (2013).
8. Pisarevsky, S., Li, Z., Tetley, M., Liu, Y. & Beardmore, J. An updated internet-based global paleomagnetic database. *Earth-Science Reviews* **235,** 104258 (2022).
9. Torsvik, T. H. *et al.* Phanerozoic polar wander, palaeogeography and dynamics. *Earth-Science Reviews* **114,** 325–368 (2012).
10. Pavlov, V. & Gallet, Y. A third superchron during the Early Paleozoic. *Episodes-Newsmagazine of the International Union of Geological Sciences* **28,** 78–84 (2005).
11. Ahanin, N. *et al.* Ordovician Reversed Superchron: Fact or Fallacy? *Earth and Planetary Science Letters* **687,** 120071 (2026).
12. Hounslow, M. W. A geomagnetic polarity timescale for the Carboniferous (2022).
13. Lanci, L. *et al.* Astronomically forced cycles in middle Permian fluvial sediments from Karoo Basin (South Africa). *Palaeogeography, Palaeoclimatology, Palaeoecology* **596,** 110973 (2022).
14. Ogg, J. in *Geologic time scale 2020* 159–192 (Elsevier, 2020).
15. Heslop, D., Roberts, A. P. & Hawkins, R. A statistical simulation of magnetic particle alignment in sediments. *Geophysical Journal International* **197,** 828–837 (2014).
16. Haigh, G. The process of magnetization by chemical change. *Philosophical Magazine* **3,** 267–286 (1958).
17. Oliver, J. Fluids expelled tectonically from orogenic belts: their role in hydrocarbon migration and other geologic phenomena. *Geology* **14,** 99–102 (1986).
18. Elmore, R. D. *et al.* Evidence for a relationship between hydrocarbons and authigenic magnetite. *Nature* **325,** 428–430 (1987).
19. Brothers, L., Engel, M. & Elmore, R. The late diagenetic conversion of pyrite to magnetite by organically complexed ferric iron. *Chemical Geology* **130,** 1–14 (1996).
20. Lu, G., McCabe, C., Hanor, J. S. & Ferrell, R. E. A genetic link between remagnetization and potassic metasomatism in the Devonian Onondaga formation, northern Appalachian basin. *Geophysical Research Letters* **18,** 2047–2050 (1991).
21. Hirt, A., Banin, A. & Gehring, A. Thermal generation of ferromagnetic minerals from iron-enriched smectites. *Geophysical Journal International* **115,** 1161–1168 (1993).
22. Katz, B., Elmore, R., Cogoini, M. & Ferry, S. Widespread chemical remagnetization: Orogenic fluids or burial diagenesis of clays? *Geology* **26,** 603–606 (1998).
23. Gallo, L. *et al.* Unraveling remagnetization sources using statistical learning. *Earth and Planetary Science Letters* **662,** 119390 (2025).
24. Hower, J., Eslinger, E. V., Hower, M. E. & Perry, E. A. Mechanism of burial metamorphism of argillaceous sediment: 1. Mineralogical and chemical evidence. *Geological Society of America Bulletin* **87,** 725–737 (1976).
25. Boles, J. R. & Franks, S. G. Clay diagenesis in Wilcox sandstones of Southwest Texas; implications of smectite diagenesis on sandstone cementation. *Journal of Sedimentary Research* **49,** 55–70 (1979).
26. Cuadros, J. & Linares, J. Experimental kinetic study of the smectite-to-illite transformation. *Geochimica et Cosmochimica Acta* **60,** 439–453 (1996).
27. Cuadros, J. Modeling of smectite illitization in burial diagenesis environments. *Geochimica et Cosmochimica Acta* **70,** 4181–4195 (2006).
28. Kars, M., Aubourg, C., Pozzi, J.-P. & Janots, D. Continuous production of nanosized magnetite through low grade burial. *Geochemistry, Geophysics, Geosystems* **13** (2012).

29. Horton, B. K. *et al.* Broken foreland basins and the influence of subduction dynamics, tectonic inheritance, and mechanical triggers. *Earth-Science Reviews* **234,** 104193 (2022).
30. Pullaiah, G., Irving, E., Buchan, K. & Dunlop, D. Magnetization changes caused by burial and uplift. *Earth and Planetary Science Letters* **28,** 133–143 (1975).
31. Kent, D. V. Thermoviscous remagnetization in some Appalachian limestones. *Geophysical Research Letters* **12,** 805–808 (1985).
32. Donardelli Bellon, U. *et al.* Clay minerals and continental-scale remagnetization: A case study of South American Neoproterozoic carbonates. *Journal of Geophysical Research: Solid Earth* **129,** e2023JB028538 (2024).
33. Pescarini, T. *et al.* Magnetic mineralogy and paleomagnetic record of the Nama Group, Namibia: Implications for the large-scale remagnetization of West Gondwanaland and its tectonic evolution. *Journal of Geophysical Research: Solid Earth* **130,** e2024JB030612 (2025).
34. Néel, L. *Théorie du trainage magnétique des ferromagnétiques en grains fins avec application aux terres cuites* in *Annales de géophysique* **5** (1949), 99–136.
35. Dunlop, D. J. & Özdemir, Ö. *Rock magnetism: fundamentals and frontiers* **3** (Cambridge university press, 1997).
36. Nagy, L. *et al.* Stability of equidimensional pseudo–single-domain magnetite over billion-year timescales. *Proceedings of the National Academy of Sciences* **114,** 10356–10360 (2017).
37. Fabian, K. & Shcherbakov, V. P. Energy barriers in three-dimensional micromagnetic models and the physics of thermoviscous magnetization. *Geophysical Journal International* **215,** 314–324 (2018).
38. Baran, R., Friedrich, A. M. & Schlunegger, F. The late Miocene to Holocene erosion pattern of the Alpine foreland basin reflects Eurasian slab unloading beneath the western Alps rather than global climate change. *Lithosphere* **6,** 124–131 (2014).
39. Yang, Z. *et al.* Sichuan Basin and beyond: Eastward foreland growth of the Tibetan Plateau from an integration of Late Cretaceous-Cenozoic fission track and (U-Th)/He ages of the eastern Tibetan Plateau, Qinling, and Daba Shan. *Journal of Geophysical Research: Solid Earth* **122,** 4712–4740 (2017).
40. Gernon, T. M. *et al.* Coevolution of craton margins and interiors during continental break-up. *Nature* **632,** 327–335 (2024).
41. Blackburn, T. J. *et al.* An exhumation history of continents over billion-year time scales. *Science* **335,** 73–76 (2012).
42. Dodson, M. H. & McClelland-Brown, E. Magnetic blocking temperatures of single-domain grains during slow cooling. *Journal of Geophysical Research: Solid Earth* **85,** 2625–2637 (1980).
43. Miller, J. D. & Kent, D. V. Regional trends in the timing of Alleghanian remagnetization in the Appalachians. *Geology* **16,** 588–591 (1988).
44. Weil, A. B. & Van der Voo, R. Insights into the mechanism for orogen-related carbonate remagnetization from growth of authigenic Fe-oxide: A scanning electron microscopy and rock magnetic study of Devonian carbonates from northern Spain. *Journal of Geophysical Research: Solid Earth* **107,** EPM–1 (2002).
45. Elliott, W. C., Basu, A., Wampler, J. M., Elmore, R. D. & Grathoff, G. H. Comparison of K-Ar ages of diagenetic illite-smectite to the age of a chemical remanent magnetization (CRM): An example from the Isle of Skye, Scotland. *Clays and Clay Minerals* **54,** 314–323 (2006).
46. Tohver, E., Weil, A., Solum, J. & Hall, C. Direct dating of carbonate remagnetization by 40Ar/39Ar analysis of the smectite–illite transformation. *Earth and Planetary Science Letters* **274,** 524–530 (2008).
47. Hower, J., Hurley, P., Pinson, W. & Fairbairn, H. The dependence of K-Ar age on the mineralogy of various particle size ranges in a shale. *Geochimica et cosmochimica acta* **27,** 405–410 (1963).
48. Hueck, M., Wemmer, K., Ksienzyk, A. K., Kuehn, R. & Vogel, N. Potential, premises, and pitfalls of interpreting illite argon dates-A case study from the German Variscides. *Earth-Science Reviews* **232,** 104133 (2022).
49. Crouzet, C., Ménard, G. & Rochette, P. High-precision three-dimensional paleothermometry derived from paleomagnetic data in an Alpine metamorphic unit. *Geology* **27,** 503–506 (1999).
50. Crouzet, C., Rochette, P. & Ménard, G. Experimental evaluation of thermal recording of successive polarities during uplift of metasediments. *Geophysical Journal International* **145,** 771–785 (2001).
51. De Groot, L. V. *et al.* Micromagnetic tomography for paleomagnetism and rock-magnetism. *Journal of Geophysical Research: Solid Earth* **126,** e2021JB022364 (2021).

52. Souza-Junior, G. F. *et al.* Robust directional analysis of magnetic microscopy images using non-linear inversion and iterative Euler deconvolution. *Journal of Geophysical Research: Solid Earth* **131,** e2025JB031725 (2026).
53. Fu, R. & Harrison, R. J. Paleomagnetic recording at the grain scale. *Elements* **22,** 111–117 (2026).
54. Torsvik, T. H. & Cocks, L. R. M. *Earth history and palaeogeography* (Cambridge University Press, 2017).
55. Vaes, B., Gallo, L. C. & van Hinsbergen, D. J. On pole position: Causes of dispersion of the paleomagnetic poles behind apparent polar wander paths. *Journal of Geophysical Research: Solid Earth* **127,** e2022JB023953 (2022).
56. Pedregosa, F. *et al.* Scikit-learn: Machine learning in Python. *the Journal of machine Learning research* **12,** 2825–2830 (2011).
57. Chuhan, F. A., Bjørlykke, K. & Lowrey, C. J. Closed-system burial diagenesis in reservoir sandstones: Examples from the Garn Formation at Haltenbanken area, offshore mid-Norway. *Journal of Sedimentary Research* **71,** 15–26 (2001).
58. Cuadros, J. & Altaner, S. P. Compositional and structural features of the octahedral sheet in mixed-layer illite/smectite from bentonites. *European Journal of Mineralogy* **10,** 111–124 (1998).
59. Środoń, J., Elsass, F., McHardy, W. & Morgan, D. Chemistry of illite-smectite inferred from TEM measurements of fundamental particles. *Clay Minerals* **27,** 137–158 (1992).
60. Cych, B., Paterson, G. A., Nagy, L. & Williams, W. First principles understanding of single domain magnetizations—Part I: the single domain comprehensive calculator (SDCC) open source library. *Geophysical Journal International* **241,** 2034–2048 (2025).
61. Reed, J. S., Spotila, J. A., Eriksson, K. A. & Bodnar, R. J. Burial and exhumation history of Pennsylvanian strata, central Appalachian basin: An integrated study. *Basin Research* **17,** 259–268 (2005).

Funding

This project has received funding from the European Research Council (ERC) under the European Union's Horizon 2020 research and innovation program (Grant agreement No. 101043844) and from the Research Council of Norway (RCN) through its Centres of Excellence funding scheme project 332523 (Centre for Planetary Habitability).

Author contributions

M.D. conceived the study. M.D. and L.C.G. analysed the paleomagnetic records. M.D. and J.T.F. developed the CRM models. M.D. and T.P. developed the TVRM models. M.D. prepared the figures and wrote the first draft of the manuscript. All authors contributed to interpreting the results and revising the manuscript.

Competing interests

The authors declare no competing interests.

Materials & Correspondence

Correspondence and requests for materials should be addressed to Mathew Domeier (mathewd@geo.uio.no)

Extended Data

Extended Data Table 1: Parameters used in the chemical remanent magnetization (CRM) and thermoviscous remanent magnetization (TVRM) models. Reference values define the baseline settings used in the models described in the main text.

Parameter	Description	Reference value	Values tested in sensitivity tests
CRM model			
b_r	Burial rate ($\mathrm{mm\,yr^{-1}}$)	0.2	0.1, 0.15, 0.2, 0.3, 0.5
G	Geothermal gradient ($^\circ\mathrm{C\,km^{-1}}$)	30	—
T_i	Initial temperature (°C)	20	—
T_f	Final temperature (°C)	300	—
Δt	Time step (yr)	200	—
S_0	Initial smectite fraction	1.0	—
K_e	Effective potassium concentration ($\mathrm{mol\,L^{-1}}$)	10^{-14}	10^{-10}, 10^{-12}, 10^{-14}, 10^{-16}, 10^{-18}
$\mathrm{SC_{mid}}$	Superchron midpoint (fraction of model time)	0.4	0.0, 0.2, 0.4, 0.6, 0.8
$\mathrm{SC_{dur}}$	Superchron duration (Myr)	37.5	20, 28.75, 37.5, 46.25, 55
TVRM model			
m_D	Median equivalent spherical diameter of the grain-volume distribution (nm)	35.53	27.00, 31.26, 35.53, 39.79, 44.05
$\sigma_{\ln V}$	Standard deviation of log grain volume	0.30	0.03, 0.15, 0.30, 0.45, 0.6
n_V	Number of grain volumes	500	—
e_r	Exhumation rate ($\mathrm{mm\,yr^{-1}}$)	0.2	0.1, 0.15, 0.2, 0.3, 0.5
G	Geothermal gradient ($^\circ\mathrm{C\,km^{-1}}$)	30	—
T_i	Initial temperature (°C)	300	—
T_f	Final temperature (°C)	20	—
Δt	Time step (yr)	200	—
B	Magnetic field strength (μT)	50	12.5, 25, 50, 100, 200
$\mathrm{SC_{mid}}$	Superchron midpoint (fraction of model time)	0.4	0.0, 0.2, 0.4, 0.6, 0.8
$\mathrm{SC_{dur}}$	Superchron duration (Myr)	37.5	20, 28.75, 37.5, 46.25, 55

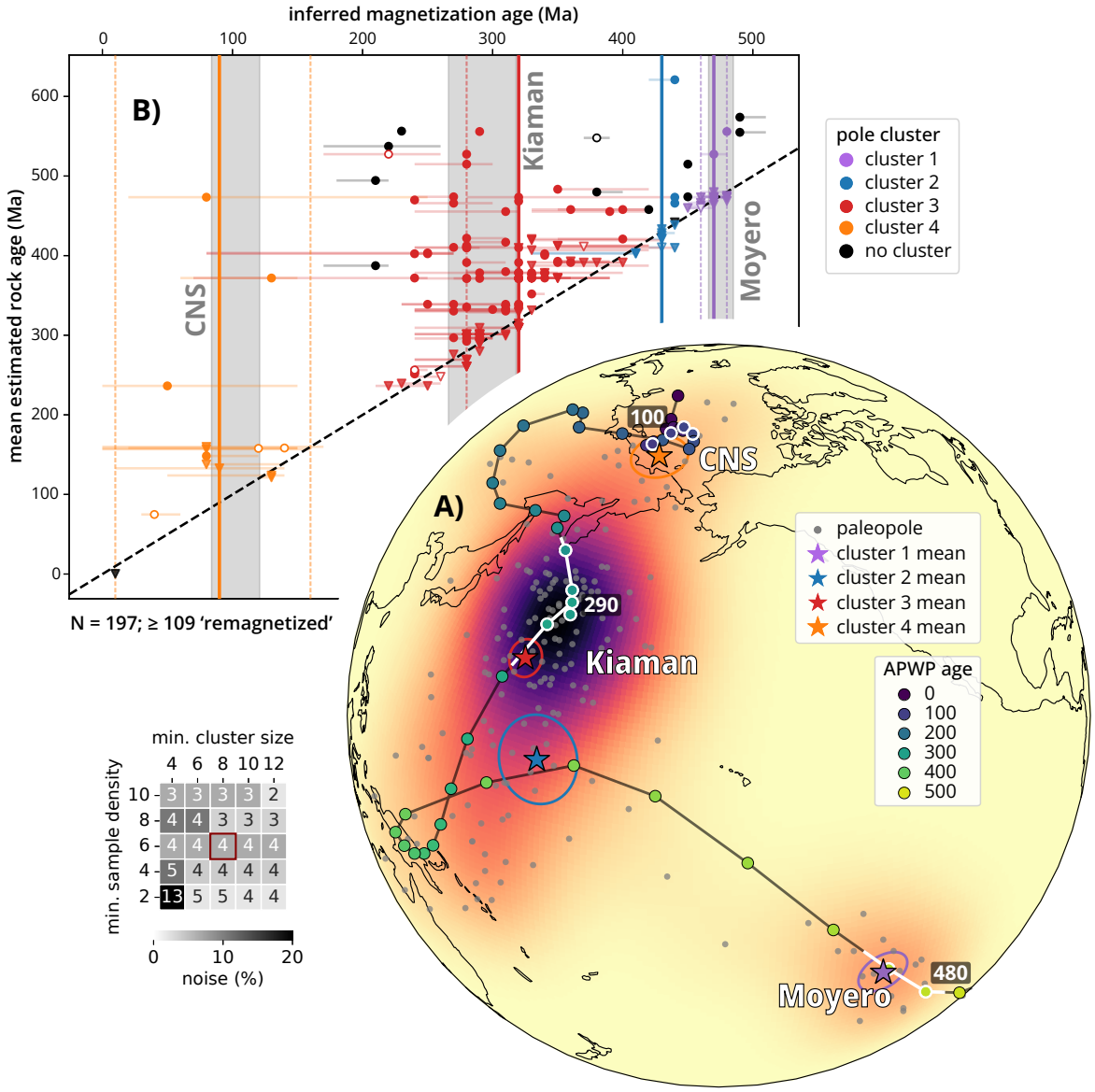

Extended Data Fig. 1: Spatiotemporal distribution of sedimentary paleomagnetic poles from Baltica. A) Spherical kernel density estimate (warm-colored background) of sedimentary paleomagnetic poles (grey points) and Fisher directional means (stars with A_{95} confidence circles) from cluster analysis on these poles, compared against the Baltican apparent polar wander path (APWP; colored circles). White segments of the path/reference poles denote the temporal ranges of the Moyero, Kiaman and Cretaceous Normal superchrons (CNS). Left inset panel shows number of clusters discovered and associated noise according to alternative cluster analysis parameters (maroon frame shows parameters used). **B)** Comparison of mean estimated ages of the rocks hosting the poles in A) vs. the best-estimate of the magnetization age based on a comparison of the pole positions against the reference APWP (see Methods). The individual poles are colored according to their cluster membership, and horizontal lines span valid magnetization ages according to APWP comparisons. Circles denote poles whose oldest valid magnetization age is younger than the age range of the host rock (e.g. remagnetized results). Downward triangles mark all other poles (e.g. possibly primary magnetizations). Open symbols show results with dual-polarities that pass a reversal test. The dashed diagonal line denotes a 1:1 age relationship. Grey intervals show the age range of superchrons, and vertical solid lines show the best-estimated age of the cluster means as determined from comparison against the reference APWP; dashed lines show the upper and lower age range of reference poles within 15° of the cluster means.

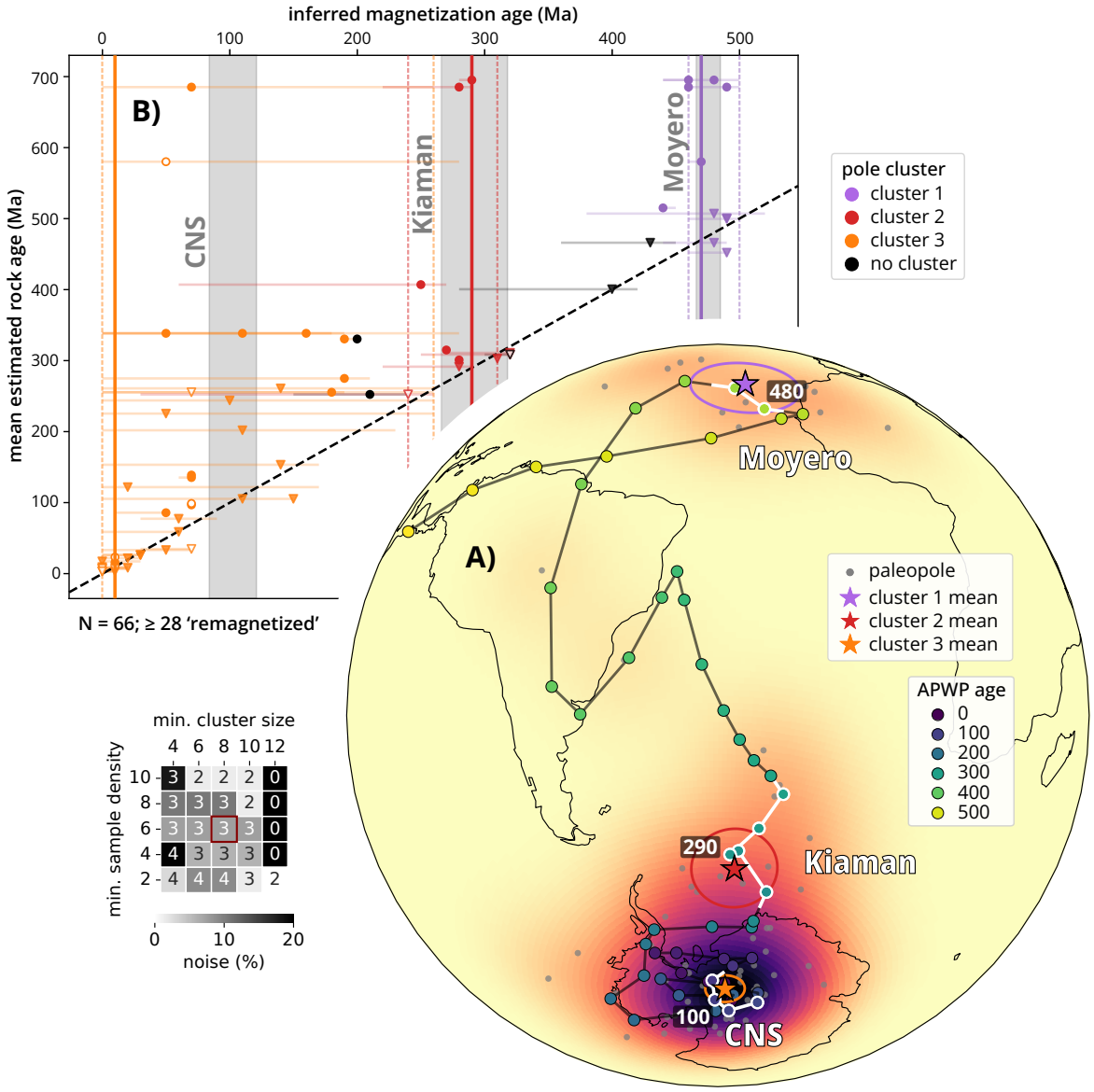

Extended Data Fig. 2: Spatiotemporal distribution of sedimentary paleomagnetic poles from Amazonia. A) and **B)** as in Extended Data Fig. 1, but for paleomagnetic poles, pole clusters and reference APWP from Amazonia.

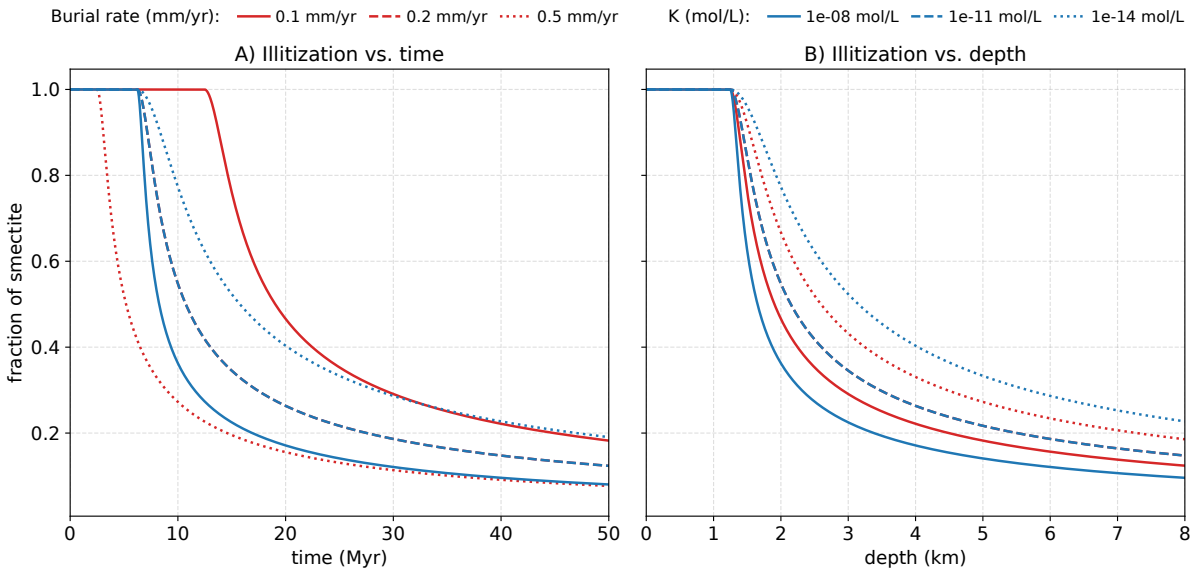

Extended Data Fig. 3: Smectite illitization under various burial rates and effective potassium concentrations. A) Illitization vs. time. **B)** Illitization vs. depth. All models use a fixed geothermal gradient of 30°C/km. Note that illitization proceeds over several tens of millions of years in all cases.

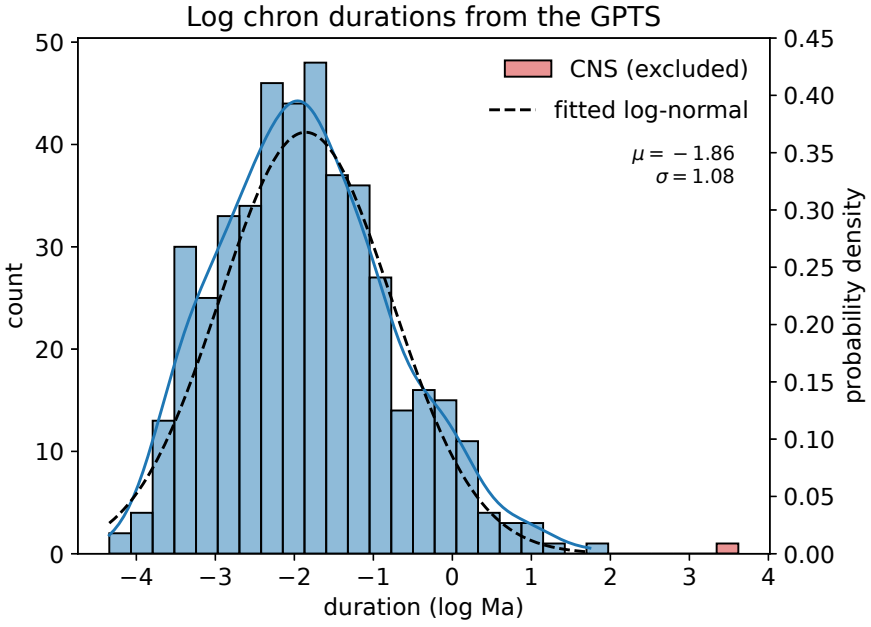

Extended Data Fig. 4: Lognormal distribution of geomagnetic polarity chron durations since 171 Ma. The chron durations were extracted from the geomagnetic polarity timescale (GPTS) of Ogg [14]. To this distribution a log-normal distribution was fitted (dashed line), after removing chron 34 (the Cretaceous Normal Superchron; red bar).

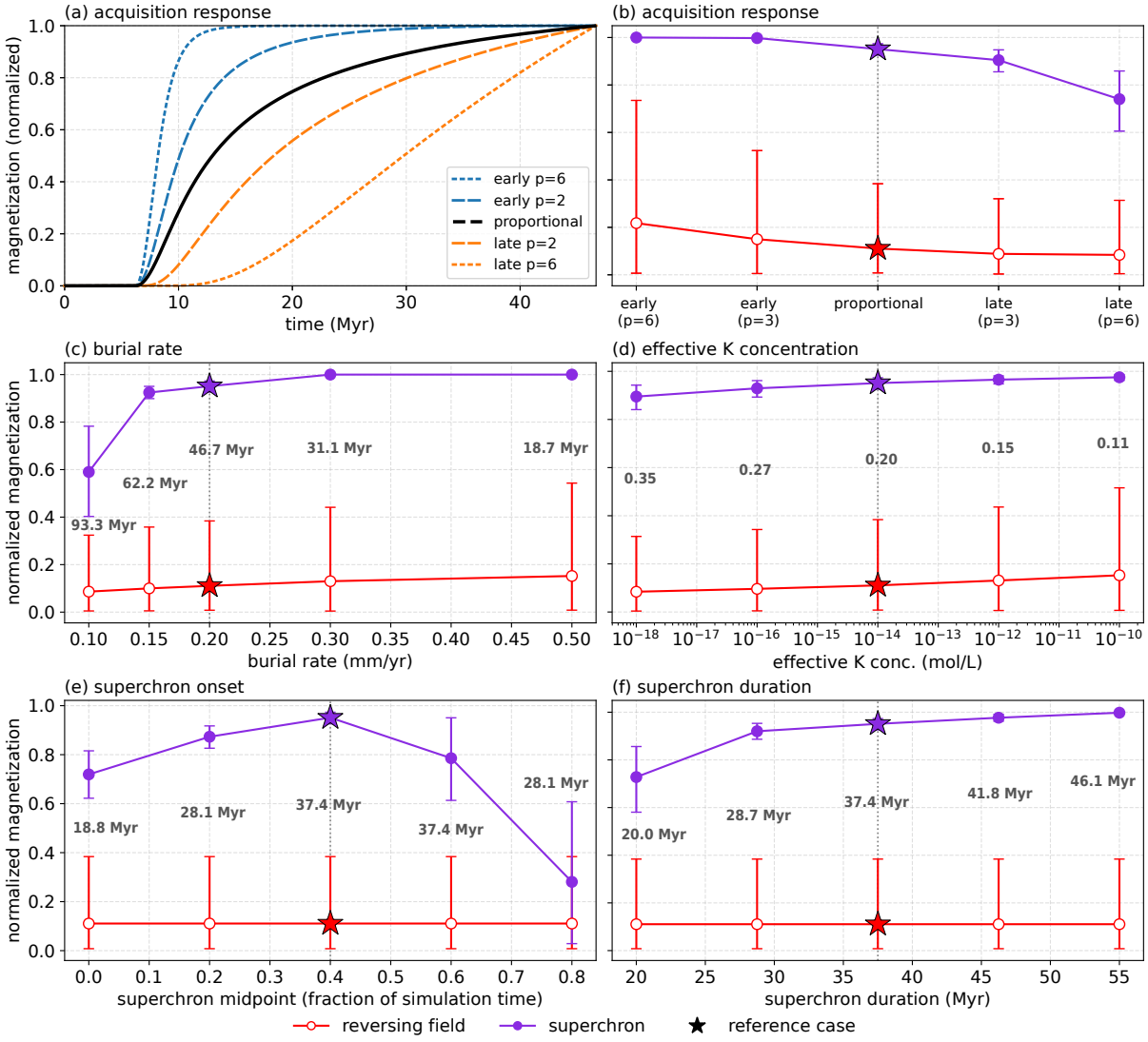

Extended Data Fig. 5: Sensitivity tests of CRM model. **a)** Different acquisition response functions applied. **b)** Effect of chosen response function. A shift towards early acquisition increases the reversing field ensemble magnetization by decreasing acquisition time, whereas a late acquisition reduces the superchron ensemble magnetization by pushing the acquisition time beyond the duration of the prescribed superchron. **c)** Effect of changing burial rate. Gray values report the time required for the system to reach $T_f = 300°C$. Slow burial delays CRM growth and pushes acquisition beyond the duration of the prescribed superchron. **d)** Effect of effective K concentration. Gray values report the smectite fraction remaining at the end of the simulation. **e)** Effect of timing of superchron onset (timing of the superchron midpoint with respect to the duration of the simulation). Gray values report the actual duration of the superchron during the simulation window. A late onset reduces the CRM acquired because most remanence is acquired early according to the reference acquisition response. **f)** Effect of superchron duration. Gray values report the actual duration of the superchron during the simulation window (the reference case places the superchron midpoint at $0.4t$ the simulation time). Note that the range spans the durations of the Moyero (19 Myr), Kiaman (52 Myr) and Cretaceous Normal (38 Myr) superchrons.

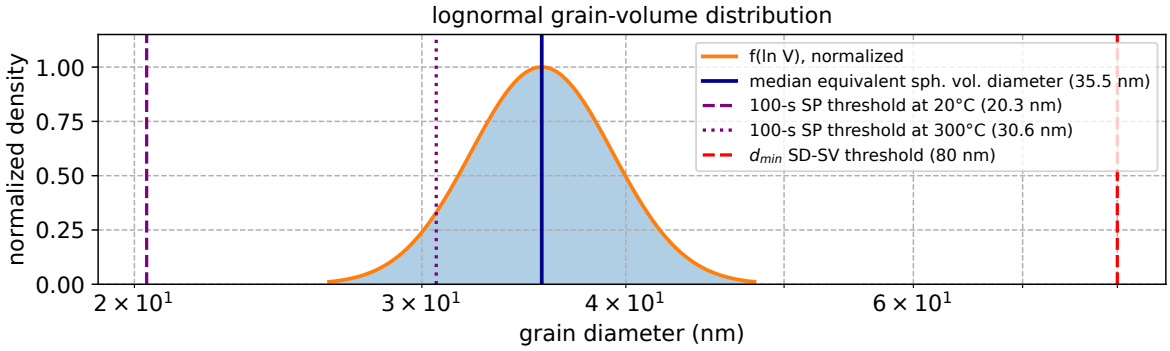

Extended Data Fig. 6: Reference lognormal grain volume distribution used in TVRM model. Superparamagnetic-single domain (SP-SD) thresholds at 20°C and 300°C are shown for reference, as well as the approximate single-domain single-vortex (SD-SV) threshold.

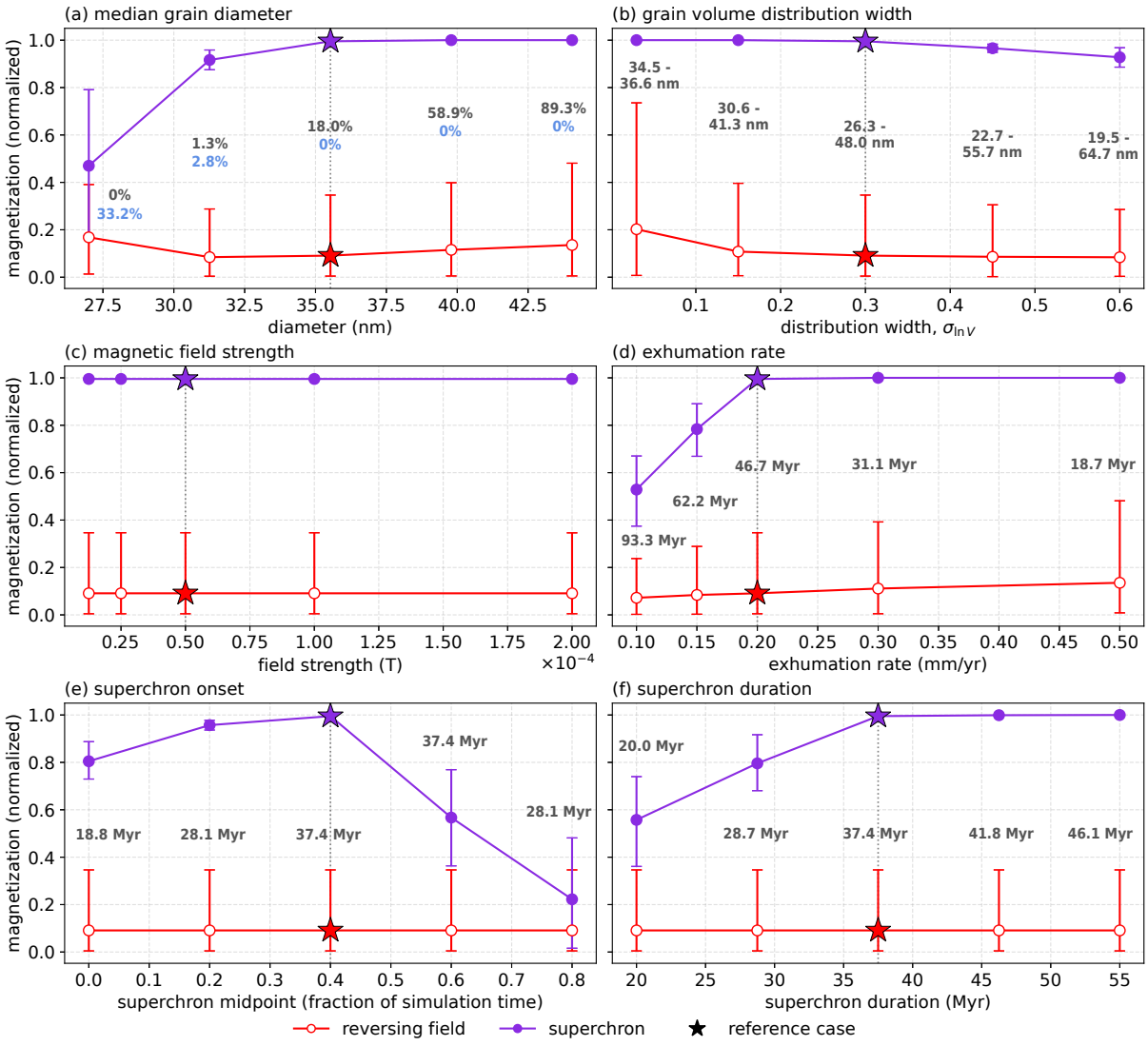

Extended Data Fig. 7: Sensitivity tests of TVRM model. a) Effect of median grain diameter. Gray values report percent of grains that are blocked at the outset (and thus excluded from the analysis), blue values report the percent of retained grains which remain unblocked (superparamagnetic) at the end of the simulation. **b)** Effect of grain volume distribution width; gray values report the range of grain diameters this corresponds to. **c)** Effect of magnetic field strength; **d)** Effect of exhumation rate. Gray values report the time required for the system to reach $T_f = 20°\text{C}$. **e)** Effect of timing of superchron onset (timing of the superchron midtpoint with respect to the duration of the simulation). Gray values report the actual duration of the superchron during the simulation window. **f)** Effect of superchron duration. Gray values report the actual duration of the superchron during the simulation window (the reference case places the superchron midpoint at $0.4t$ the simulation time).